Second Harmonic Generation Confocal Microscopy of Collagen Type I from Rat Tendon Cryosections

Theodossis A. Theodossiou,* Christopher Thrasivoulou,† Chidi Ekwobi,† and David L. Becker†
*Department of Medicine, The Rayne Institute, University College London, London, United Kingdom; and †Centre for Cell and Molecular Dynamics, Department of Anatomy and Developmental Biology, University College London, London, United Kingdom

ABSTRACT We performed second harmonic generation (SHG) imaging of collagen in rat-tendon cryosections, using femtosecond laser scanning confocal microscopy, both in backscattering and transmission geometries. SHG transmission images of collagen fibers were spatially resolved due to a coherent, directional SHG component. This effect was enhanced with the use of an index-matching fluid ($n_i = 1.52$). The average SHG intensity oscillated with wavelength in the backscattered geometry (isotropic SHG component), whereas the spectral profile was consistent with quasi-phase-matching conditions in transmission geometry (forward propagating, coherent SHG component) around 440 nm ($\lambda_p = 880$ nm). Collagen type I from bovine Achilles tendon was imaged for SHG in the backscattered geometry and its first-order effective nonlinear coefficient was determined ($|d_{eff}| \approx 0.085(\pm 0.025) \times 10^{-12} mV^{-1}$) by comparison to samples of inorganic materials with known effective nonlinear coefficients (LiNbO3 and LiIO3). The SHG spectral response of collagen type I from bovine Achilles tendon matched that of the rat-tendon cryosections in backscattered geometry. Collagen types I, II, and VI powders (nonfibrous) did not show any detectable SHG, indicating a lack of noncentrosymmetric crystalline structure at the molecular level. The various stages of collagen thermal denaturation were investigated in rat-tendon cryosections using SHG and bright-field imaging. Thermal denaturation resulted in the gradual destruction of the SHG signal.

INTRODUCTION

After the invention of the ruby laser, the effect of optical second harmonic generation (SHG) was observed as the production of ultraviolet light ($\lambda = 347$ nm) when ruby laser irradiation ($\lambda = 694$ nm) traversed a quartz crystal (1). Since then, SHG has found applications in various scientific fields. The principle of this nonlinear optical phenomenon lies in the annihilation of two photons and the creation of a single one at double the frequency in materials with first-order nonlinear susceptibility. Unlike two-photon excited fluorescence, SHG is not a resonant phenomenon, and thus SHG is temporally coincident with the pumping beam. The intensity of the second harmonic signal bears a quadratic dependence on the intensity of the pumping radiation, since SHG is a second-order (first-order nonlinear) effect. In transparent, highly organized birefringent materials, such as noncentrosymmetric crystals, SHG production employs phase matching with the pumping radiation through an oo-e or ee-o interaction, and thus the SHG is coherent and propagates forward utilizing the whole length of the medium. However, in scattering nonlinear media, the SHG produced is phase-mismatched and its intensity oscillates with depth. An extensive overview of the theory lying behind the phenomenon of SHG can be found in bibliography (2–6).

The first report of SHG in biological tissues, to the best of our knowledge, is by Vasilenko et al. (7), who reported visual observation of infrared laser emission consistent with second harmonic generation in the human eye. This phenomenon was further investigated and corroborated by others later (8–10).

The first demonstration of second harmonic generation in biological systems, however, came from Fine and Hansen (11) with the use of a Q-switched ruby laser. Since then, numerous research groups have demonstrated second harmonic generation in a variety of tissues containing collagen, both in the nanosecond regime (12–15) and in the picosecond and femtosecond regimes with the use of ultrafast laser technology (16–20). Although several other tissue components were identified as sources of SHG (16,17), collagen, shown to possess a triclinic microcrystalline structure by Bragg reflections in its x-ray diffraction pattern (21), was identified as the most efficient SHG source in tissue (15–17).

Collagen is the most widespread of the structural proteins in higher vertebrates, and in its native form three peptide chains are arranged in a rod-shaped, triple-helix tertiary conformation. Helix-coil transition induced by heating has been investigated with various techniques including differential scanning calorimetry, spectrophotometry of turbidity, scanning microcalorimetry, and NMR (22–25). During the denaturation process the microcrystalline structure of collagen is destroyed, and hence the ability to produce optical second harmonic is gradually lost, resulting in decreased SHG intensity (17,26,27). The denaturation trend of collagen has been found to be consistent with previous results by differential scanning calorimetry and highly dependent on the collagen type and origin (27).

Submitted July 21, 2006, and accepted for publication September 13, 2006.
Address reprint requests to Theodossis A Theodossiou, Dept. of Medicine, The Rayne Institute, 5 University St., University College London, London WC1E 6JJ, UK. Tel.: 30-69-48-922-616; E-mail: t.theodossiou@gmail.com.

0006-3495/06/12/4665/13 $2.00
doi: 10.1529/biophysj.106.093740

Although the first attempts of a combination of SHG and microscopy were on nonbiological samples (28,29), Freund and co-workers (14) used SHG microscopy to image rat-tail tendon samples, showing that collagen fibers formed highly polar structures at the 50-μm resolution scale of their system. Moreux and co-workers (30) used second harmonic microscopy to image membranes and experimentally verify their calculations of various parameters for nonlinear membrane imaging. SHG and two-photon fluorescence microscopy were combined for imaging of rabbit cornea in the backscattering geometry, and SHG tomography was employed to assess the collagen content of the corneal stroma (31). Three-dimensional SHG imaging of various endogenous structural proteins, such as myosin and tubilin, has been performed on biological tissues and compared to two-photon fluorescence (TPF) imaging (32,33). This combination of SHG and TPF imaging was also employed in a study of organotypic RAFT collagen type I tissue model. The wavelength and depth dependence of the SHG signal was investigated in this model (34). Confocal SHG imaging of human endometrium, kangaroo-tail tendon, and liver cryosections was performed at high resolution. The diagnostic value of SHG to liver cirrhosis was demonstrated (35). SHG imaging of collagen in tumors has revealed an SHG intensity correlation for different types of tumors consistent with their collagen-content ratio. According to the same study, pharmacological intervention proved to have an effect similar to that of collagenases to the SHG signal in tumors (36). Second harmonic and two-photon microscopy performed on uniform-polarity microtubule assemblies have shown that SHG can be a powerful tool in the investigation of kinetics and function of microtubule ensemble polarity in dynamic native brain tissue structures (37). In a recent work by Zipfel and co-workers (38), second harmonic generation and two-photon microscopy were also used to image several collagen-containing tissues; the potential of SHG in the diagnosis of diseases such as cancer and Alzheimer's was outlined. Elsewhere, hyperplastic parenchyma was successfully differentiated from normal stromal tissue using SHG microscopy (39).

The main aim of this study was to characterize the SHG properties of collagen using a high-resolution, confocal microscope, with a view to developing a novel technique for wound/scar analysis. Principally, SHG imaging was performed on rat-tendon cryosections of near optical quality both in backscattering and transmission geometries. Power dependence and spectral compliance of the acquired SHG images with the pumping laser radiation was assessed, whereas wavelength dependence of the SHG signal was investigated and modeled between 415 and 455 nm. Images of thermal denaturation of collagen were obtained using both SHG and bright-field imaging. Opaque collagen type I samples versus opaque lithium niobate and lithium iodate powder samples, imaged in backscattering geometry were employed to approximate a value for the SHG coefficient of collagen type I.

MATERIALS AND METHODS

Sample preparation

Tendon was freshly harvested from the hind-limb paws of adult female Wistar rats. The Tendon was mounted in cryoprotectant, cryosectioned longtitudinally at 20 μm, and mounted onto glass slides. Due to the morphology of the original sample the exact sectioning angle was impossible to determine. Before imaging, the samples were mounted in either phosphate-buffered saline (PBS) or index-matching fluid (LS5252, $n_i = 1.52$, sample gift from Lightspan, Wareham, MA) and covered with No. 1 coverslips.

The polymerized collagen fibers of collagen type I from bovine Achilles tendon (27662, Fluka, Buchs, Switzerland) were mounted on microscope slides and coverslipped. Due to the optically opaque nature of this sample, imaging was only performed in the backscattering geometry. Several other collagen samples in powder (nonfibrous) form were imaged in the same manner, namely collagen type I from calf skin (C9791, Sigma-Aldrich, St. Louis, MO), collagen type I from rat tail (Sigma-Aldrich C7661), collagen type II from chicken sternum cartilage (Sigma-Aldrich C9301) and collagen type VI from human placenta (Sigma-Aldrich C7521).

For backscattering SHG imaging, optically opaque layers of lithium niobate ($LiNbO_3$) and lithium iodate ($LiIO_3$), in powder form (Sigma-Aldrich 254296 and 443964, respectively) were placed on microscope slides, with coverslips pressed on top of the samples to ensure the smoothest possible surface morphology.

Experimental setup

The experimental setup is outlined in Fig. 1. The laser used for generation of second harmonic was a mode-locked femtosecond/picosecond Ti:Sapphire Tsunami (Spectra-Physics, Mountain View, CA) synchronously pumped by a Millenia VII (Spectra-Physics) diode-pumped solid-state frequency-doubled laser capable of delivering up to 8.5 W pumping power at 532 nm.

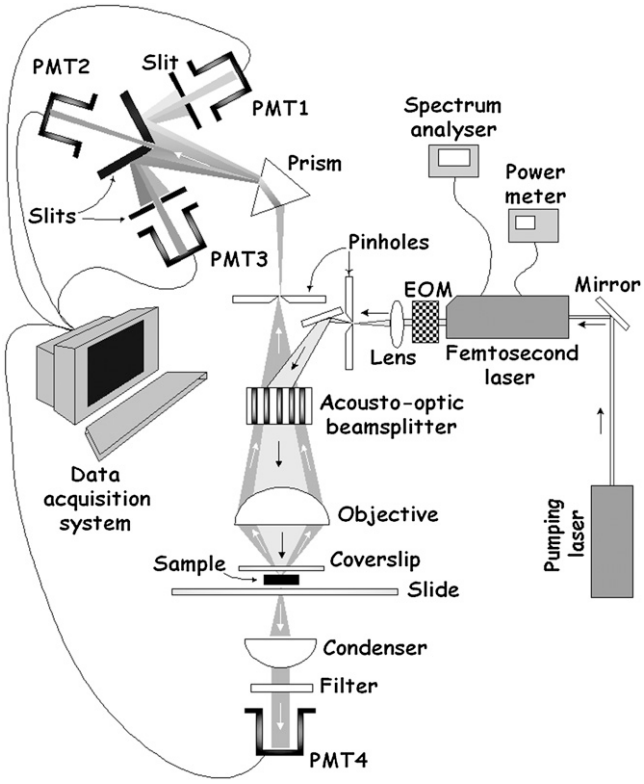

FIGURE 1 Experimental setup.

The Tsunami laser, tunable between 700 and 1000 nm, consistently produced pulses of 80 fs width between 840 and 920 nm. Pulse repetition rate was registered as 80.7 MHz with the use of a Startek 1350 frequency counter (Startek International, Ft. Lauderdale, FL), and the average power at different wavelengths was recorded by a Spectra-Physics 407a power meter. Wavelength identification and selection was made possible with the use of an IST laser spectrum analyzer (IST, Horseheads, NY) coupled to a TDS 210 oscilloscope (Tektronix, Beaverton, OR). The Tsunami laser output was fed to an electro-optical modulator (EOM LIV20, Linos, Göttingen, Germany) before being coupled to the confocal microscope, so that laser intensity control and optimization to the microscope objective could be achieved.

The confocal system used was a Leica TCS SP2 acousto-optic beamsplitter (AOBS) multiphoton confocal laser scanning microscope (Leica, Milton Keynes, UK) coupled to a Leica DMRE upright microscope, and the lens used throughout the experiments was a 40×, 1.25 NA, Panfluor, oil-immersion objective. All SHG imaging in the backscattered geometry was performed in the descanned detector with the maximum confocal pinhole setting at 600 μm. Control experiments were performed to ensure that there was no loss of SHG signal at this confocal pinhole size. We found no appreciable loss of SHG signal as the confocal pinhole was reduced to 500 μm (98% of maximum pinhole reading). Upon entering the Leica microscope system, the Tsunami beam was expanded and passed through a programmable AOBS, capable of single and multichroic beam splitting and subsequently focused through the objective lens to an estimated beam diameter of 0.14 μm ($\lambda_p = 880$ nm). The backscattered emission from the sample was collected trough the objective lens and delivered through the AOBS and the detection pinhole to the prism spectrophotometer detection system via the spectral dispersion prism. The dispersed spectrum was focused by a lens into a central programmable slit, which defined the part of the emission to be detected by photomultiplier tube 2 (PMT2). The rest of the emission was reflected to photomultipliers 1 (PMT1) and 3 (PMT3), again through programmable slits. The width of the slits in front of each PMT could be software-adjusted so that each PMT could detect spectral regions spanning from a 5-nm bandwidth up to the overall spectral capacity of the system (400–800 nm). The gain of the PMTs could also be software-adjusted for optimized detection, avoiding saturation. The overall optical detection range with this arrangement was limited to 400–800 nm because of the chromatic aberrations within the objectives and prism between the ultraviolet and visible spectra. Therefore, we were unable to detect SHG in the region between 700-nm and 830-nm laser excitation (SHG 350–415 nm) due to the detection limitations. At the other end of the spectrum, the near-infrared water-absorption region affected laser stability at 930 nm (SHG 465 nm), although we were able to record a roll-off of SHG at 925 nm. Registration of SHG in the region above 925 nm was unachievable. In transmission geometry, a fourth PMT (PMT4) detected emission via the microscope condenser from the sample. PMT4 was identical to the three PMTs in the descanned configuration. All the PMTs (R6357, Hamamatsu, Shizuoka, Japan) present a wavelength-independent response in the spectral region of 400–500 nm.

The average power of laser irradiation after the microscope objective was measured with the use of a thermopile power meter (PM140, Gentec Electro-Optics, Quebec, Canada), unless otherwise stated. In this manner, the power at the microscope objective was calibrated to the Tsunami output power at nine wavelengths from 830 to 910 nm, with a step of 10 nm. This calibration was performed at 100% EOM voltage with parameters such as the PMT gain/black level or the pinhole diameter remaining unchanged. The pumping power was consistently maintained below the damage threshold of the samples, which for the thin rat tendon sections was found to be at an intensity of 1.5×10^8 W cm^{-2}.

Unless otherwise stated, image resolution was set to 1024 × 1024 pixels at 8-bit gray depth.

SHG verification

To ensure that the images acquired were second-harmonic images, several precautions were taken. Throughout our experiments, the SHG images in reflection mode were collected with use of the PMT2 with a band-width adjustment allowing collection in a spectral region of 5 nm on either side of the central SHG wavelength. In reflection mode, PMTs 1 and 3 were used to scan the spectrum on either side of the SHG registration band between 400 and 800 nm. No detectable emission was registered outside of the SHG registration band, confirming that our SHG signal was not due to other spurious emissions, e.g., autofluorescence of the sample. Since our experiments were restricted to the 830–910 nm spectral region (415–455 nm for the SHG signal) a short-pass filter with cut-off at 500 nm (Corion LS-500, Corion, Franklin, MA) was placed in front of the transmission PMT detector (PMT4) throughout the SHG imaging experiments. The filter had an average peak transmittance of 70% in the spectral region 410–490 nm, whereas the transmittance dropped to <0.001 of the peak transmittance for wavelengths $\geq$600 nm.

A power dependence on the pumping radiation for the SHG images was established both in transmission and reflection acquisition mode (see Fig. 3 *A*). This was achieved by varying the power of the laser, without changing any other experimental parameters, at the fundamental wavelength of 880 nm, while imaging the same field on the sample slide. The image emission matrix was thus registered and averaged to yield a mean value in regions of interest selected to exclude the majority of the dark pixels. The values of the regions of interest were averaged to yield a mean value, and a standard deviation was used as the error value. The selected regions of interest were maintained unchanged throughout the series of acquired images. The logarithms of the means were plotted against the logarithms of the laser power at the microscope objective calibrated to the registered laser output power, as detailed earlier. Thus, the power dependence of the SHG on the pumping intensity was reflected by the slopes of the linear fits.

An emission λ-scan was performed at 880-nm laser excitation (see Fig. 3 *B*) at a peak pumping intensity of 0.4×10^8 W cm^{-2}. PMT1 slits were adjusted to a detection bandwidth of 5 nm and were scanned in 18 steps across the spectral region between 420 and 450 nm. The λ-scan could only be performed in the backscattering geometry.

SHG wavelength dependence

The SHG dependence on wavelength was investigated for all samples. For the rat-tendon samples, wavelength dependence of the second harmonic signal was registered both in backscattered and transmission geometry due to the near optical quality of the samples The procedure was performed for samples in both the PBS environment and the LS 5252 index-matching fluid. For the bovine Achilles tendon collagen, the wavelength dependence of the SHG was established in opaque samples, and hence only in backscattering geometry, since the sample was opaque and light could not traverse the specimen. The SHG spectra were collected at five angles of fibril orientation on the plane of the optical axis, namely, 0°, 22°, 45°, 67°, and 90°. It must be noted here that at the 0° orientation the fibril long axis was perpendicular to the laser polarization, whereas at the 90° orientation the fibril long axis was parallel to the laser polarization (see Fig. 5).

The laser was tuned between 830 and 910 nm at 10-nm steps, with the peak intensity maintained at 0.4×10^8 W cm^{-2} at all times. The SHG images were obtained in a spectral detection window each time, spanning 5 nm either side of the central SHG wavelength. The EOM voltage was set to 100%. Regions of interest in the resulting images were selected and processed as detailed above, and the mean values plotted against wavelength comprised the wavelength response of the SHG.

Thermal denaturation

The thermal denaturation of rat-tendon cryosections was studied at 880-nm laser excitation. The pumping peak intensity was maintained at 0.4×10^8 W cm^{-2}, whereas SHG imaging was performed within the spectral band of 435–445 nm. The rat sections were initially imaged at a stabilized temperature of 25°C. A SHG image was taken followed by a bright-field

transmission image using the 488-nm argon laser line. The samples were then immersed for 5 min (to achieve thermal equilibrium) in a water bath stabilized at 50°C and the same field of view was sequentially reimaged for SHG and bright-field transmission, with experimental settings identical to those used previously. The procedure was repeated at 60° and 70°C.

Estimation of the effective nonlinearity d_{eff} for collagen type I

Samples of opaque collagen type I from bovine Achilles tendon, lithium niobate powder, and the collagen type I, II, and VI powders were prepared as described in Sample preparation. The SHG images were obtained at 880 nm with a pumping intensity of $I_p = 0.4 \times 10^8$ W cm^{-2}. Sequential image acquisition was performed to collect the relative reflected light from the samples using the 488-nm laser. The backscattering images were collected in geometry identical to that of the SHG image but this time in the spectral region 483–493 nm. The 488-nm argon line was used in lieu of the 458-nm argon line absent in our system, as it was the laser line closest to the SHG wavelength for 880-nm pumping (440 nm). Both the SHG and the backscattering images were processed as previously described, i.e., several regions of the images were used to obtain average powers and the mean of these was calculated. The error of the SHG intensity and backscattering intensity is in each case presented as the standard deviation of the mean.

The second harmonic intensity in backscattering geometry for optically opaque samples is given by (18)

$$I_{2\omega} \propto 16\pi(\omega^2/n^2_{\omega\text{-o}} n_{2\omega\text{-e}} c^2)\kappa S^2_{2\omega} |d^2_{\text{eff}}| I^2_{\omega}. \quad (1)$$

In this equation, ω is the fundamental frequency, $n_{\omega-o}$ and $n_{2\omega\text{-e}}$ are the refractive indexes at ω (ordinary) and 2ω (extraordinary), respectively, c is the speed of light, κ is a function related to particle size, $S_{2\omega}$ is the backscattering coefficient at 2ω, d_{eff} is the effective nonlinearity, and I_ω is the intensity of the pumping beam. From this, it is easy to derive a relation between the effective nonlinearities between two samples A and B:

$$|d_{\text{effA}}| = |d_{\text{effB}}| \cdot \sqrt{\frac{I^{\text{A}}_{2\omega}}{I^{\text{B}}_{2\omega}}} \cdot \frac{n^{A}_{\omega\text{-o}} \sqrt{n^{\text{A}}_{2\omega\text{-e}}}}{n^{\text{B}}_{\omega\text{-o}} \sqrt{n^{\text{B}}_{2\omega\text{-e}}}} \cdot \frac{S^{\text{B}}_{2\omega}}{S^{\text{A}}_{2\omega}} \sqrt{\frac{\kappa^{\text{B}}}{\kappa^{\text{A}}}}. \quad (2)$$

In this equation, we approximated the factor $(S^{\text{B}}_{2\omega}/S^{\text{A}}_{2\omega})\sqrt{\kappa^{\text{B}}/\kappa^{\text{A}}}$ with the experimental quantity $(I^{\text{B}}_{\text{backscatter}}/I^{\text{A}}_{\text{backscatter}})^{1/2}$.

RESULTS

Imaging of rat-tendon cryosections

Rat-tendon cryosection samples were prepared and imaged for SHG as detailed in Materials and Methods. The resulting images of the rat-tendon sections mounted in PBS environment appear in Fig. 2. In this figure, images *A–C* were obtained with a 3× zoom, whereas images *D–F* were obtained with a 5× zoom. Images *A* and *D* were acquired in backscattering geometry and images *B* and *E* in transmission geometry; images *C* and *F* are two-color renditions of the backscattering and transmission images.

It is clear from Fig. 2 that the transmission images produce finer detail of the collagen matrix structure, as individual polar fiber formations can be seen. A power dependence test was performed, as detailed in Materials and Methods, for both backscattering and transmission geometry images. The results appear in Fig. 3 *A*, and the linear regressions applied to the log-log plots revealed a quadratic power dependence of SHG intensity to the power intensity ($I_{\text{SHG}} \propto I^{2.1}_{\text{pump}}$ for backscattering collection geometry and $I_{\text{SHG}} \propto I^{1.9}_{\text{pump}}$ for transmission geometry. The error to the fitted exponents was ±0.2 in both cases, as calculated from the least-squares regression to the log-log plot).

Data from the emission wavelength scan (λ-scan) of the SHG image in the backscattering geometry appear in Fig. 3 *B*. The data in this graph were fitted to a Gaussian curve exhibiting a maximum at 440 nm (half the pumping wavelength of 880 nm). The full width at half-maximum of the Gaussian distribution (~10 nm) obeys a $1/\sqrt{2}$ relationship to

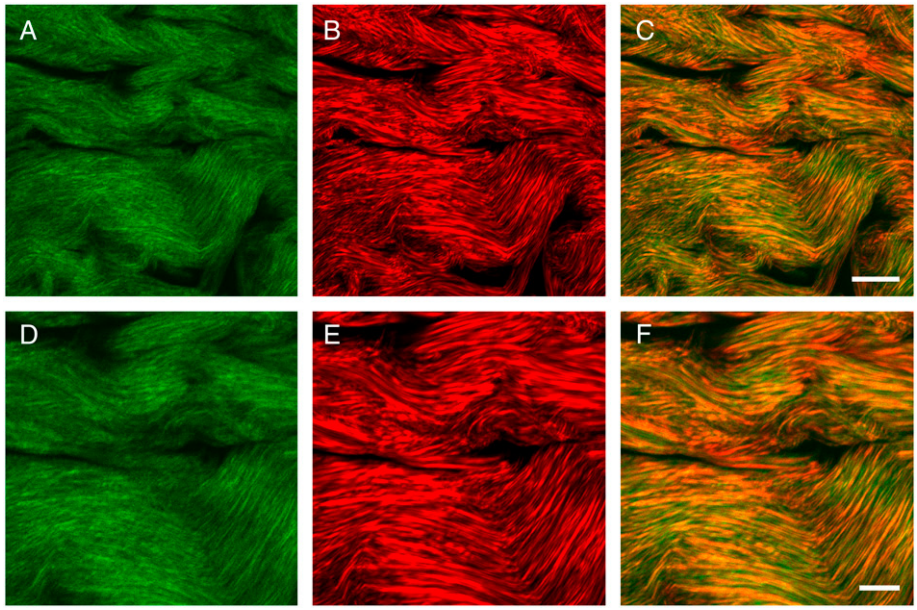

FIGURE 2 SHG imaging of collagen in 20 μm rat-foot flexor tendon cryosections mounted in PBS. The pumping wavelength was 880 nm and the SHG in backscatter geometry was imaged between 435 and 445 nm. (*A*) SHG in backscattering geometry (3× zoom). (*B*) SHG collected in transmission geometry (3× zoom). (*C*) Two-color overlay of images *A* and *B* (scale bar, 20 μm). Images *D–F* are the corresponding images for a 5× zoom (scale bar, 10 μm).

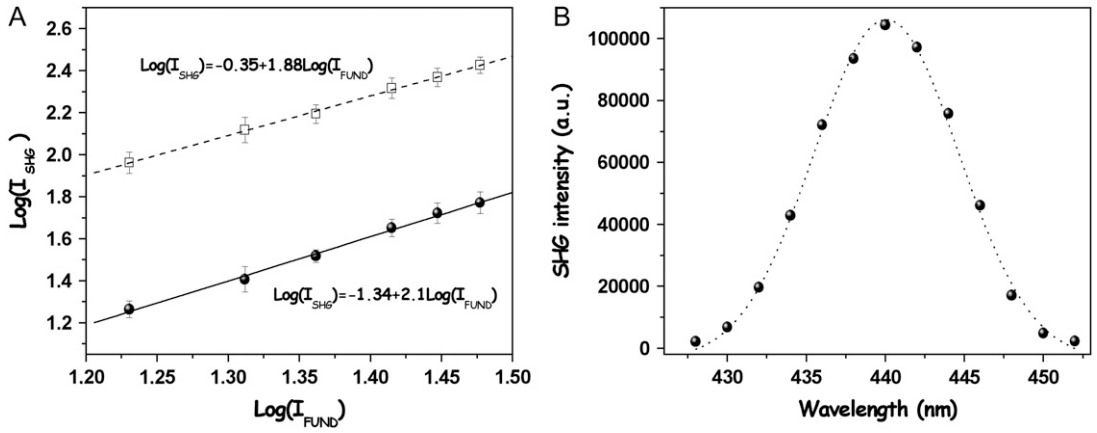

FIGURE 3 (*A*) Log-log plot of the SHG intensity derived from SHG imaging of rat-tendon cryosections versus pumping intensity ($\lambda_p = 880$ nm). Solid spheres and solid line correspond to SHG data acquired in the backscatter geometry, whereas open squares and dashed line represent the SHG data registered in transmission geometry. (*B*) Emission λ-scan of the SHG signal ($\lambda_p = 880$ nm) acquired from SHG imaging on rat-tendon cryosections. The dotted line represents a Gaussian fit. The full width at half-maximum of the fitted curve bears a $1/\sqrt{2}$ relation to the spectral profile of the corresponding beam.

the corresponding wavelength profile of the fundamental beam (~14 nm).

The data in Fig. 3 demonstrate that the images acquired are of second-order nature and, more specifically, illustrate frequency doubling of the fundamental beam.

Fig. 4, *A* and *B*, shows high-power SHG images (zoom 5×) taken in backscattering and transmission geometries, respectively, for rat-tendon cryosections in LS 5252 index-matching fluid. Fig. 4 *C* is the overlay of these two images. It is evident that in comparison to PBS-immersed samples, the backscattering image is more diffuse. In contrast, the transmission image is far better resolved and the polar fibrillar collagen structure is more coherent. Fig. 4 *D* shows the SHG intensity ratios of the backscattering images with/without index-matching fluid (*solid line*) and the corresponding SHG intensity ratio of the transmission images (*dashed line*). The wavelength scan was performed as detailed in the relevant Materials and Methods subsection. The ratio of transmitted SHG with/without index-matching fluid presents an interesting wavelength response, as shown earlier in the graph of

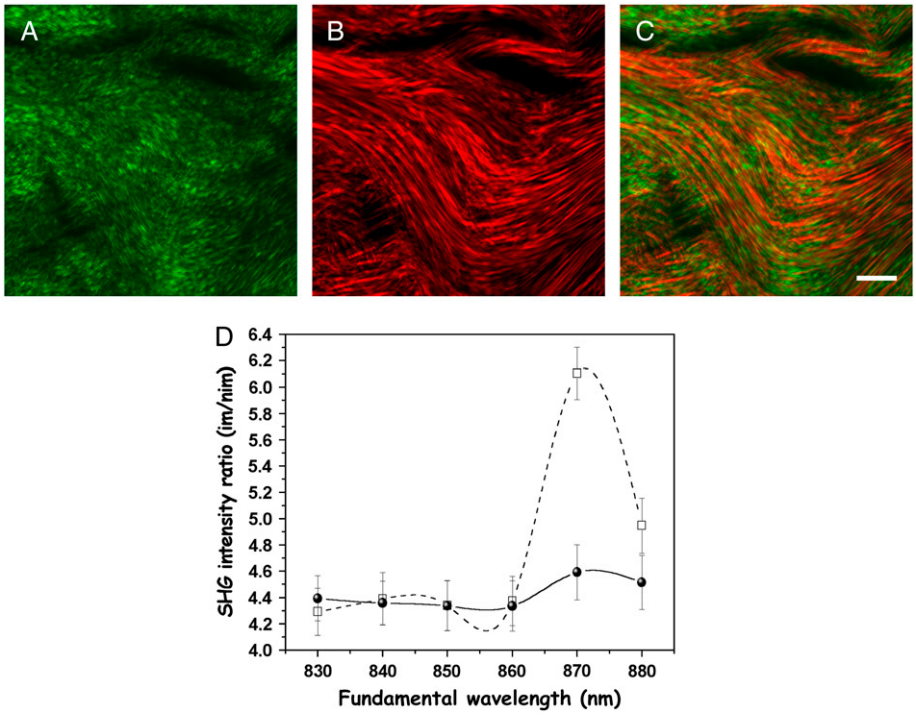

FIGURE 4 SHG imaging ($\lambda_p = 880$ nm) of collagen in rat-tendon cryosections mounted in index matching fluid ($n_i = 1.52$). (*A*) Backscatter geometry (SHG acquisition between 435 and 445 nm). (*B*) Transmission geometry (through the LS-500 filter). (*C*) Two-color rendition of the overlay of *A* and *B* (5× zoom, scale bar, 10 μm). (*D*) SHG intensity ratio with/without index matching fluid versus wavelength. The solid curve represents backscatter geometry data, whereas the dashed curve represents transmission geometry data.

Fig. 4 *D*. The calculated ratio between index-matched and non-index-matched immersion fluids lies between 4.3- and 4.9-fold-increased intensity in the spectral region 415–430 nm and increases significantly to a 6.2-fold increase at 435 nm. The corresponding ratio for the backscattering collection geometry remains between 4.3- and 4.6-fold for the whole wavelength range.

The forward (transmitted) coherent SHG signal in non-centrosymmetric crystals is described by:

$$I_{2\omega} \propto \frac{d_{\text{eff}}^2 L^2 I_\omega^2}{n_{\omega\text{-o}}^2 n_{2\omega\text{-e}} \lambda^2} \times \frac{\sin^2[2\pi\lambda^{-1} L\delta n]}{[2\pi\lambda^{-1} L\delta n]^2}, \quad (3)$$

where λ is the fundamental frequency, $\delta n = n_{\omega\text{-o}} - n_{2\omega\text{-e}}$ is the dispersion introduced by the difference of the refractive indexes at ω (ordinary) and 2ω (extraordinary), respectively, d_{eff} is the effective nonlinearity, I_ω is the intensity of the pumping beam, and L is the length of the crystal. The $\sin^2$ term is the measure of phase-matching between the fundamental and the double-frequency radiation. In a completely phase-matched situation, when $n_{2\omega\text{-e}} = n_{\omega\text{-o}}$, this term becomes unity and the SHG is maximized for the whole length of the crystal. In our system, an additional dispersion is introduced by the scattering properties of collagen, as well as by the refractive index mismatch in the objective-medium sample complex.

Wavelength dependence of SHG

The wavelength dependence of SHG in the spectral region between 830 and 910 nm for rat-tendon cryosections was investigated both in transmission and backscattering geometries. The resulting graphs for samples imaged in PBS environment appear in Fig. 5, *A* and *B*, for all five angles of fibril orientation (0°, 22°, 45°, 67°, and 90°). In Fig. 5, *C* and *D*, the images for the angles 0° and 90°, respectively, are shown. On these figures, the yellow arrows represent laser polarization, whereas the cyan arrows represent the fibril longitudinal axis.

Fig. 5 *A* represents the transmitted SHG signal after the 500-nm-cutoff short-pass filter in front of the detection PMT,

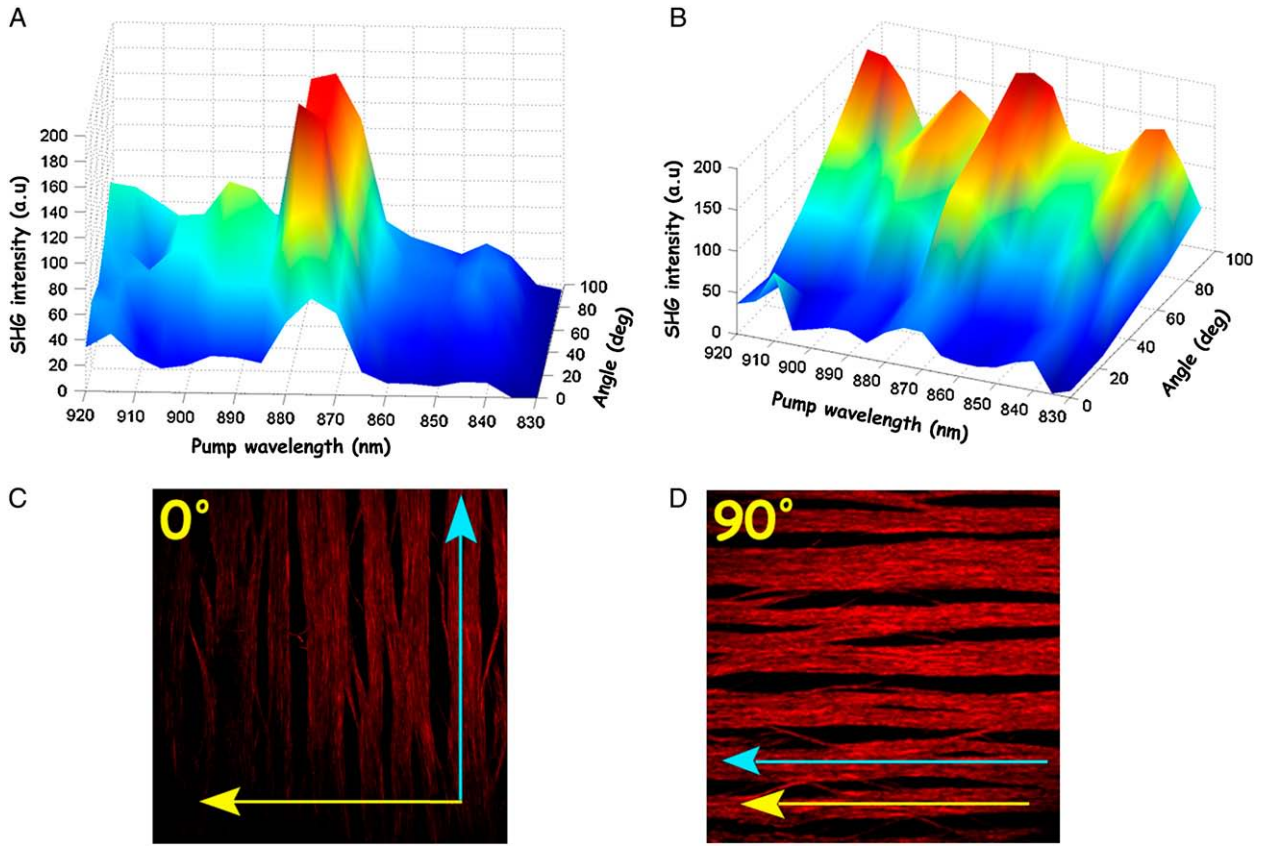

FIGURE 5 Wavelength response of the SHG intensity in rat-tendon cryosections (λ_p,880 nm) for various fibril orientation angles (0°, 22°, 45°, 67°, and 90°). (*A*) Transmission geometry. (*B*) Backscatter geometry. (*C*) SHG image (transmission) of 0° collagen-fibril long-axis orientation. (*D*) Same field as in *C* rotated by 90°. The yellow arrows in *C* and *D* represent the laser polarization. Cyan arrows denote the collagen-fibril longitudinal axis. Although the intensity scales in *A* and *B* appear comparable, the intensity in transmission geometry (*A*) is ~50 times higher due to different PMT settings. The power calibration after the microscope objective for the data in Fig. 5 was performed with a wavelength-corrected Coherent (Santa Clara, CA) OP2-VIS power meter.

whereas Fig. 5 *B* represents the backscattered SHG wavelength dependence. Although the two spectra seem to be in comparable scales, the intensity of the transmitted geometry is ~50 times higher due to different PMT settings. The transmitted SHG spectrum exhibits one maximum around 880 nm while the intensity for all wavelengths increases monotonously with the angle (0→90°). There are also three secondary maxima around the wavelengths of 845, 895, and 915 nm.

In the backscattered geometry (Fig. 5 *B*), there are four maxima of comparable intensities at 845, 880, 895, and 915 nm. As in the case of transmission geometry, the SHG intensity exhibits a monotonous increase with the angle (0→90°) for all wavelengths. The corresponding wavelength response for samples imaged in LS 5252 index-matching fluid (data not shown) are not statistically different from those shown in Fig. 5.

The normalized wavelength dependence of the backscattered signal in the bovine Achilles tendon sample is shown in Fig. 6. The solid curve represents the spectral profile of SHG emitted from the bovine Achilles tendon collagen sample, whereas the dashed curve is the spectral profile of the rat-tendon cryosections in backscattering geometry (data from Fig. 5, 90°) also presented here for comparison.

From this figure, it can be seen that the collagen type I bovine Achilles tendon SHG data collected in backscattering geometry is similar to the wavelength response of backscatter SHG from rat-tendon cryosections. Sample rotation in the optical axis plane made no statistically significant difference in terms of SHG intensity for the Achiles tendon collagen type I, $LiNbO_3$, and $LiIO_3$ samples.

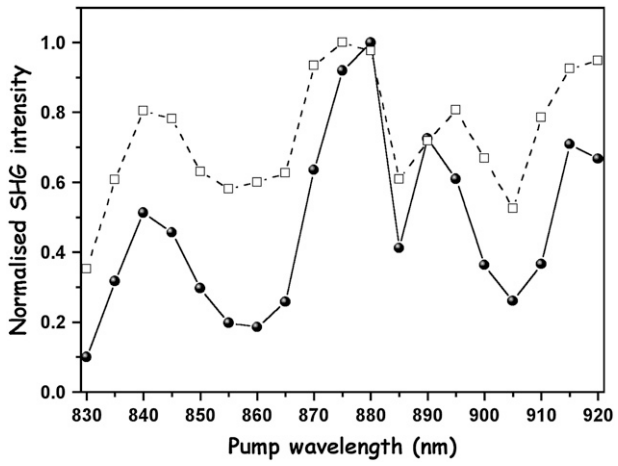

FIGURE 6 Wavelength response of the normalized SHG in collagen type I from bovine Achilles tendon (*solid curve with solid spheres*). The SHG spectral response of rat-tendon cryosection collagen is also shown (*dashed curve with open squares*) for comparison. Both SHG signals were derived in the backscattered geometry ($\lambda_p = 830$–910 nm). The power calibration after the microscope objective for the data in Fig. 6 was performed with a wavelength-corrected Coherent OP2-VIS power meter.

Estimation of the effective nonlinearity d_{eff} for collagen type I

Samples of opaque collagen type I from bovine Achilles tendon, lithium niobate powder, and lithium iodate powder, as well as the collagen powders from other species, were imaged both for SHG (pumping wavelength 880 nm) and single-photon backscattering at 488 nm, as described in Materials and Methods. In Fig. 7, the SHG images for collagen type I from bovine Achilles tendon (*A*) and lithium niobate (*B*) are shown. The SHG intensities in the two images are not displayed on a relative scale, since the gain of the PMT was set to a different level to avoid saturation (SHG intensity from lithium niobate was higher by a factor of 6.3×10^3). The collagen powder samples (type I, type II, and type VI) did not produce any detectable SHG.

As detailed in Materials and Methods, in Eq. 2 we approximated the factor $(S^{B}_{2\omega}S^{A}_{2\omega})\sqrt{\kappa^{B}\kappa^{A}}$ with the experimental quantity $(I^{B}_{scatt2\omega}/I^{A}_{scatt2\omega})^{1/2}$ to facilitate calculation of the nonlinear coefficient of collagen. In this context, Eq. 2 becomes, for our purposes,

$$|d^{A}_{eff}| = |d^{B}_{eff}| \times \sqrt{\frac{I^{A}_{SHG}}{I^{B}_{SHG}}} \times \frac{n^{A}_{\omega\text{-o}}\sqrt{n^{A}_{2\omega\text{-e}}}}{n^{B}_{\omega\text{-o}}\sqrt{n^{B}_{2\omega\text{-e}}}} \times \sqrt{\frac{I^{B}_{scatt2\omega}}{I^{A}_{scatt2\omega}}}. \quad (4)$$

This method of determination was initially validated using samples of $LiNbO_3$ and $LiIO_3$, for which the absolute values of nonlinear optical coefficients are well documented in the references (5,6).

For $LiNbO_3$, we calculated the respective values for the refractive indices from the Sellmeier equations (40) as $n^{LN}_{\omega\text{-o}} = 2.274$, $n^{LN}_{2\omega\text{-e}} = 2.288$, whereas for $LiIO_3$ we used the values $n^{LI}_{\omega\text{-o}} = 1.868$ and $n^{LI}_{2\omega\text{-e}} = 1.760$ (41). In this manner, we obtained $|d^{LiIO3}_{eff}| = 0.9(\pm 0.1) \times |d^{LiNbO3}_{eff}|$.

For collagen type I from bovine Achilles tendon we approximated the values of the refractive indices at ω and 2ω with the value of the group refractive index of collagen I (42), so that $n^{C}_{\omega\text{-o}} \approx n^{C}_{2\omega\text{-e}} \approx 1.5$. In this fashion, we obtained from Eq. 4 $|d^{Coll}_{eff}| = 0.020(\pm 0.008) \times |d^{LiNBO3}_{eff}|$.

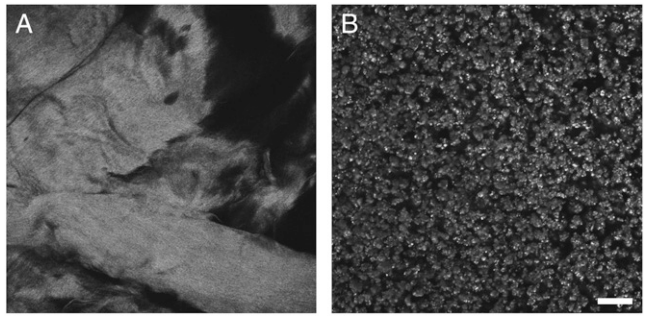

FIGURE 7 SHG images of (*A*) collagen type I from bovine Achilles tendon and (*B*) lithium niobate powder (scale bar, 40 μm). Both images were acquired between 435 and 445 nm in the backscattered geometry ($\lambda_p = 880$ nm).

In terms of absolute values, if we substitute $|d_{\text{eff}}^{\text{LiNbO3}}| = |d_{31}| = 4.3\times10^{-12}\text{mV}^{-1}$(6), we have $|d_{\text{eff}}^{\text{CollI}}| \approx 0.085\ (\pm0.025)\times10^{-12}\text{mV}^{-1}$.

Thermal denaturation

Experiments on the effects to the SHG signal after thermal denaturation of collagen were performed according to the protocol detailed in Materials and Methods. The resulting SHG images for both backscattering (Fig. 8, *A*, *D*, *G*, and *J*) and transmission (Fig. 8, *B*, *E*, *H*, and *K*) geometries are shown in Fig. 8, along with the bright-field images (Fig. 8, *C*, *F*, *I*, and *L*), for each temperature (25°, 50°, 60°, and 70°C, respectively).

The denaturation process in collagen seems to be taking place in two steps. From 25° to 50°C, there is a loss of SHG intensity but the fiber morphology appears to be maintained. At 60°C, there is a loss of SHG intensity accompanied by shrinking and partial loss of collagen content. At 70°C, the whole of the collagen content denatured, turning into gelatin (as clearly seen from the bright-field image in Fig. 8 *L*) and no SHG is detectable either in backscattering or transmission geometry.

The change in the average SHG intensity during the denaturation process is quantified in Fig. 9. The data in Fig. 9 represent the mean values of average SHG intensity from various regions of interest in the corresponding SHG images, whereas the errors represent the standard deviation of the mean.

DISCUSSION

In recent years, SHG has become a powerful diagnostic tool in biomedicine, especially with regard to tissue with high collagen content (35–37,39), but also to myosin-rich muscle sarcomeres (52) and skeletal muscle (53).

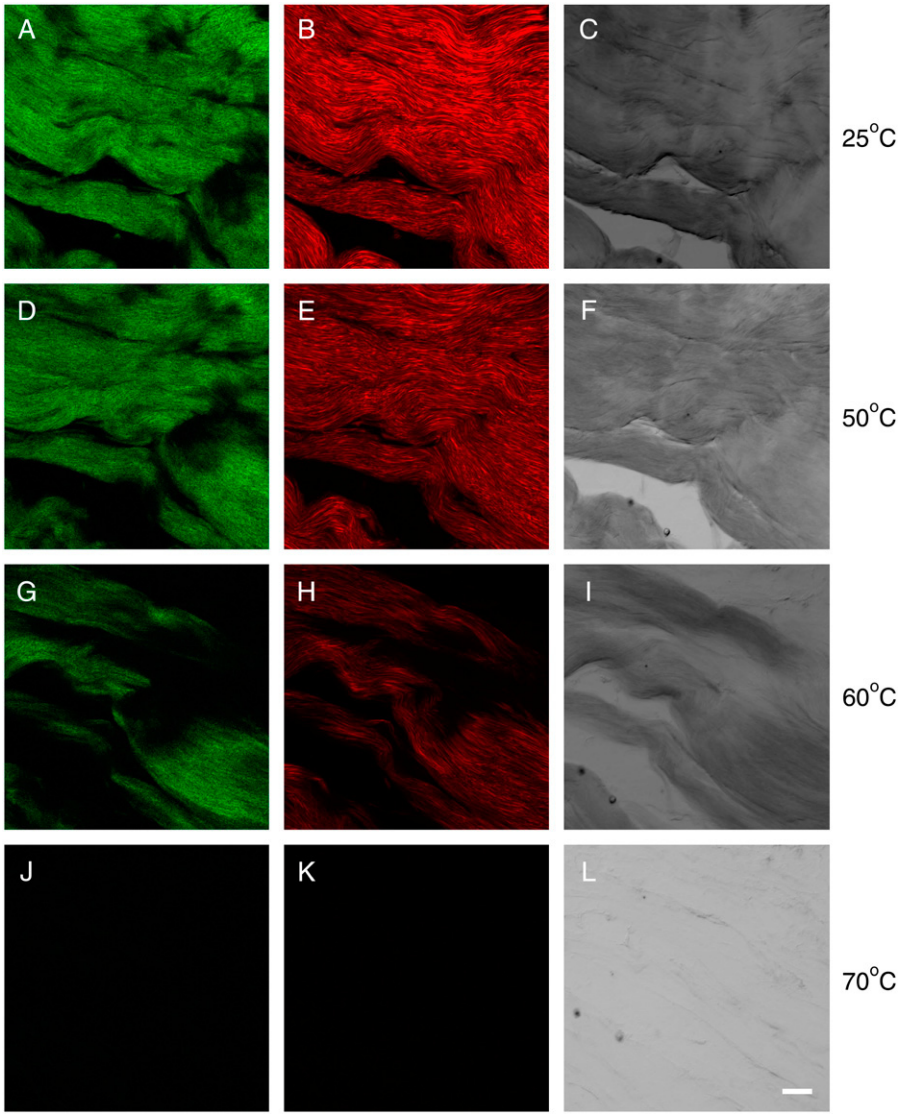

FIGURE 8 SHG imaging ($\lambda_p = 880$ nm) of collagen thermal denaturation in rat-tendon cryosections and the corresponding bright-field images (*C*, *F*, *I*, and *L*) ($\lambda = 488$ nm). The SHG images in backscatter geometry (*A*, *D*, *G*, and *J*) were collected in the spectral bandwidth 435–445 nm. Corresponding SHG transmission images (*B*, *E*, *H*, and *K*) were collected via the 500-nm short-pass filter. Beginning at top, rows of images (backscatter SHG, transmission SHG, and bright-field, respectively) correspond to native collagen at 25°C (*A–C*) and 50°C (*D–F*), significant thermal denaturation of collagen at 60°C (*G–I*), and, finally, denatured collagen at 70°C (*J–L*) (scale bar, 40 μm).

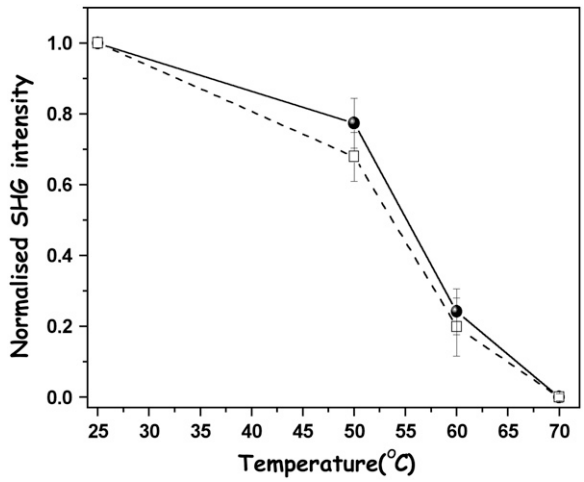

FIGURE 9 SHG intensity versus temperature as derived from the images in Fig. 8. Solid spheres and solid line represent the SHG data collected in backscatter geometry, whereas open squares and dashed line represent SHG data collected in transmission geometry.

Although a clinical application of SHG as an in vivo diagnostic tool would have to rely on the backscattering component due to the turbid nature of tissue, a considerable part of the SHG microscopy work has been performed in transmission geometry (32,33,35,37). In this work, we performed SHG confocal microscopy on rat-tendon cryosections to compare the SHG images collected in backscattering and transmission geometries. In Fig. 2, the rat-tendon cryosections were imaged both in backscattering (*A* and *D*) and transmission (*B* and *E*) geometries, using different zoom values of 3× and 5×, respectively. Upon comparison, SHG in the backscattered image is of a more diffuse nature, but the collagen fibrillar bundle organization is still evident. In the transmission geometry, however, polar collagen fibrils are clearly distinguishable within the collagen bundles, as shown by the two-color renditions (Fig. 2, *C* and *F*). This effect is due to a forward-propagating coherent SHG component in the transmission images derived from the crystalline structure of the collagen fibers, in contrast to the collective SHG signal from the collagen fiber bundles in backscattered geometry. This effect is enhanced with the use of an index-matching fluid, as will be discussed below.

In the case of the rat tendons, since they are thin sections of near-optical quality, Eq. 3 applies to both backscattered and transmitted SHG. However, the transmitted SHG consists of two components: one coherent, directional forward-moving component with better spatial resolution and one scattered isotropic component. The isotropic component behaves similarly to the backscattered component ''oscillating'' with wavelength, as shown in Fig. 6. A similar oscillatory pattern has been shown with varying material length L in phase-mismatched conditions, both in crystals (43) and, most importantly, in homogeneous nonlinear media in reflection geometry (44). The backscattered SHG signal from collagen type I from bovine Achilles tendon opaque samples exhibits a wavelength dependence that is quite similar to that of the rat-tendon cryosections in the backscattering geometry. This indicates that SHG from type I collagen has a unique wavelength profile irrespective of fiber polarity. Rat-tendon sections exhibit polar formations of collagen fibers, whereas in the bovine Achilles tendon sample the collagen fibers are interwoven in a more or less chaotic fashion, as suggested by the SHG images in Figs. 2 *A* and 7 *A*, respectively.

In Eq. 3, the factor $(\sin^2[2\pi\lambda^{-1}L\delta n]/[2\pi\lambda^{-1}L\delta n]^2)$ becomes 1, by application of L'Hôpital's theorem from calculus, when $\delta n = 0$.

As rigorously described by Yariv (5), since the extraordinary refractive index of the second-harmonic component is a function of angle ($n_{2\omega\text{-e}} = n_{2\omega\text{-e}}(\theta)$), the factor $2\pi\lambda^{-1}L(n_{2\omega\text{-e}} - n_{\omega\text{-o}})$ of Eq. 3 can be expressed (by expanding $n_{2\omega\text{-e}}(\theta)$ as a Taylor series near the root $\theta \approx \theta_m$) as $\beta(\theta - \theta_m)$ and consequently $I_{SHG}(\theta) \propto (\sin^2[\beta(\theta - \theta_m)]/[\beta(\theta - \theta_m)]^2)$. This was verified by Ashkin et al. (45), as their experimental data were successfully fitted to $(\sin^2[\beta(\theta - \theta_m)]/[\beta(\theta - \theta_m)]^2)$, showing phase matching at $\theta \approx \theta_m$. In nonlinear crystals, $\theta \approx \theta_m$ supports phase matching at a unique $\lambda \approx \lambda_m$ and crystals are cut at different angles for frequency doubling at different wavelengths.

Following the above rationale, and since δn is a function of wavelength through the corresponding Sellmeier equations, there is a root $\lambda \approx \lambda_m$ around which we could perform a Taylor series expansion (assuming perfect phase matching at $\lambda = \lambda_m$) and thus obtain $I_{SHG}(\lambda) \propto (\sin^2[\beta(\lambda - \lambda_m)]/[\beta(\lambda - \lambda_m)]^2)$. The analytical derivation of β is beyond the scope of this manuscript and could be subject to further theoretical considerations once the specific Sellmeier constants of collagen become available. However, β will be a function of L, λ_m, and the Sellmeier constants. We have fitted the data in Fig. 5 for the forward-scattering geometry to $(\sin^2[\beta(\lambda - \lambda_m)]/[\beta(\lambda - \lambda_m)]^2)$ and the fit yielded $\lambda = 877 \pm 1$. It is hence obvious that at ~880 nm there is quasi-phase matching in the forward direction within the thickness of our sample.

The increasing intensity with rotation ($0 \rightarrow 90°$) on the optical axis plane, observed in Fig. 5, *A* and *B*, is a polarization effect similar to what was previously described (14,17). The SHG signal is stronger when the fibril long axis is parallel to the laser polarization and is minimized when that axis becomes perpendicular to the laser polarization.

In Fig. 6, the spectra of the backscattered SHG from both our tendon samples and the opaque collagen I sample are in good spectral agreement and both signify phase mismatching. Equation 3 applies to a focused beam. In the case of the fundamental beam transversing a crystal, the Gaussian beam is characterized by confocal parameter z_0, which is the distance from the beam waist at which the beam area is double that of the beam waist. Equation 3 is valid if the beam is focused so that $2z_0 = L$ (crystal length). In our case, given the

NA of our objective (1.25), Eq. 3 can be applied to a length of ± 265 nm either side of the focal point (beam waist 140 nm). In any case, the possibility of SHG effects (or any multiphoton effects) outside this region is negligible. In this sense, our coherent second harmonic is only generated within this volume (double cone) around the focal point, and subsequently propagates forward, mainly depleted by scattering. The coherent component at the sample interface (detected by the transmission detector) remains phase-matched, as $2z_0$ and the remaining sample thickness are both less than or equal to the coherence length of collagen ($\sim 10\ \mu$m, according to Roth and Freund (12)). The weaker (due to the low scattering probability within the thickness of our samples) forward and backward isotropically scattered components are, on the other hand, of approximately equal intensity. In the Achilles tendon collagen samples, correspondingly, the weaker backscattered component mainly emanates from depth equal to or smaller than the coherence length of the sample, which again is comparable to the thickness of our tendon cryosections.

Quasi-phase matching in our samples is corroborated by index matching; the index-matching fluid used has a refractive index of 1.52, consistent with the group refractive index of collagen type I (12,42). The use of the index-matching fluid further enhances the optical quality of our rat-tendon samples, rendering in them a more crystal-like behavior. In the absence of phase matching (as in the case of the backscattered SHG), the improvement is, within experimental error, expected to be uniform across the spectrum (Fig. 4 *D*, *solid line*). However, in the transmission geometry, the ratio of transmitted SHG intensity with/without index matching fluid in Fig. 4 *D* remains at $\sim$4.5 for pumping wavelengths between 830 and 860 nm, whereas it reaches a maximum ratio value of over 6.2 between 870 and 880 nm (*dotted line*). This is consistent with a further enhancement of the phase-matching conditions between the fundamental and SHG components at these wavelengths. The results from the use of the index-matching fluid further support our choice of a refractive index value of 1.5 for collagen type I in our calculation of its effective nonlinear coefficient.

To the best of our knowledge, phase matching in biological tissues has only been briefly addressed, in the study by Kim et al. (19). Their arguments involve the refractive index difference between 800 nm (fundamental beam) and 400 nm (second-harmonic component), which they compare with the birefringence-related refractive index difference of collagen fibers. In that context, their conclusions could only apply to pumping radiation at 800 nm and SHG at 400 nm. Furthermore, the refractive indices used therein are group refractive indices for tissue (blood, liver, adipose, muscle, kidney, lung, and spleen—and not collagen) taken from work by Bolin et al. (46), and do not represent the extraordinary-ordinary interaction, which could be involved in phase-matching considerations. For example, although the difference between the ordinary refractive indices of KH_2PO_4 (KDP) at 2000 and 1000 nm is 0.036, the corresponding difference between the ordinary refractive index at 2000 nm and the extraordinary refractive index at 1000 nm is 0.0009 (47). In any case, the argument presented in the work by Kim et al. could only apply to biological tissue where they claim that the refractive index difference between the fundamental and second-harmonic components is too big (0.03–0.08) for phase matching to occur. They quote, however, a much smaller refractive index difference resulting from the birefringence of collagen fibers (0.003), which in fact supports the possibility of phase matching in collagen.

Our wavelength model of SHG in tendon cryosections is in good agreement with the theoretical principles of SHG. However, there is still some controversy in this field with regard to wavelength response of collagen generated second harmonic. The study by Zoumi et al. (34) is the only previous attempt to model the SHG spectral profile of collagen, to the best of our knowledge, and is incompatible with the model presented herein. On the other hand, Zipfel et al. (38) have produced a spectral profile of collagen SHG in the spectral region between 740 and 920 nm. We cannot comment on the spectral response they present below the 800 nm point, due to our system's limitations, described in Materials and Methods. We can only suggest, however, the possibility of resonant enhancement of SHG in the short-wavelength region. In any case, the data presented by Zipfel et al. are incompatible with the model and data by Zoumi et al. (34), as also noted in the published manuscript by Zipfel et al. (38).

The collagen powders (types I, II, and VI) did not exhibit any SHG, although it should be noted that these are not powders in the classical free-flowing sense, but are lyophilized nonfibrous trimeric collagen. Collagen type I from bovine Achilles tendon, which was also optically opaque but with fibrous structure, exhibited quite efficient second-harmonic generation. This sample had an added benefit of acting as control, to verify the composition of the main collagen type found in our rat-tendon sample. In addition, both $LiNbO_3$ and $LiIO_3$ fine polycrystalline powders frequency-doubled the incident fundamental radiation quite efficiently. This suggests that the SHG properties of collagen mainly derive from its macroscopic fibrillar structure rather than its microcrystalline molecular structure. This argument is also supported by a recent study showing efficient third-harmonic generation (THG) from collagen in solution (48). Unlike SHG, which vanishes in centrosymmetric systems due to symmetry considerations, THG is efficiently produced in both centrosymmetric and noncentrosymmetric crystals, although as the beam focus gets tighter the Gouy phase shift causes THG to decrease, despite the increase of the fundamental intensity at the focus. To the best of our knowledge, there is no equivalent study for SHG in collagen solutions and our efforts to study SHG in both collagen powders and gels, where collagen exists in trimeric form, yielded no

detectable SHG signal. This indicates that only polymerized collagen fibers form an SHG efficient noncentrosymetric system.

SHG investigation in crystalline powders of various inorganic materials has previously been performed for the evaluation of their first-order optical nonlinearity (49). Although in that work a parabolic reflector or an integrating sphere ensured efficient collection of SHG, in our system the collection geometry remained unaltered for all samples to enable a direct comparison among the materials investigated. Our derivation of the first-order nonlinear coefficient of collagen type I is strongly supported by the successful correlation of the nonlinear coefficients of $LiNbO_3$ and $LiIO_3$ by the same method. Since both the lithium niobate and lithium iodate samples are in polycrystalline form and since the collagen type I from bovine Achilles tendon sample is made up of randomly oriented collagen fibers, our considerations with respect to the d_{eff} are independent of polarization considerations. The derived d_{eff} is a convolution of the two polarization components ($P_{\perp}$ and $P_{\parallel}$ to the fibril axis (20,50)). The obtained effective nonlinear coefficient for collagen type I is quite high, as it is $\sim$0.4 that of KDP, a commercially used frequency doubler. This calculation is consistent with a previous estimate of the effective nonlinear coefficient of collagen type I (17). In that work, the authors used a picosecond Nd:YAG laser at 1064 nm to correlate the I_{SHG} of collagen with that of a 3-mm KDP crystal. They thus estimated the d_{eff} of collagen as $d_{\text{eff}} \approx 0.3\times10^{-12}\text{mV}^{-1}$ (17). Furthermore, the previous study by Roth and Freund (12) provides a calculation of the effective susceptibility of rat-tail-tendon collagen, which is compatible with our derivation.

The tertiary structure of collagen is that of a rod-shaped triple helix formed by the convolution of three amino acid chains. Upon thermal denaturation, this conformation changes into the form of three loose strands or one strand and a residual β-helix, both characteristic of gelatin. This transformation is known as the helix-coil transition. The images in Fig. 8 show this transition for rat-tendon cryosections through SHG imaging. The bright-field images corroborate the gradual gelatinification of the collagen samples. As detailed in Results, this transformation seems to take place in two stages. From 25° to 50°C, the SHG signal is diminished by $\sim$25%. However, at 60°C some of the collagen is destroyed and in the remaining collagen bundles the SHG signal is further diminished. The overall SHG signal shows a decrease of 80–85% from the native state at 25°C. Finally, the whole collagen content is denatured at 70°C, and no SHG signal is detected from the sample. The denaturation results are consistent with previous studies (17,26,27). Work similar to this was performed by Lin et al. (51), which is in good agreement with our work. These observations have clinical importance, since diathermy is regularly used for tissue bisection during surgery and may result in collagen damage leading to impaired wound healing.

Our group has developed a unique treatment to accelerate wound healing, which involves a transient knockdown of connexin 43, based on ODN technology and applied locally to the wound site (54). Although our wound-healing project is part of an ongoing study, and the results are not included herein, we can report that we have successfully demonstrated that SHG imaging can be used to assess the quality of wound closure by performing scar analysis based on SHG imaging of collagen in and around the wound in both transmitting and backscattering geometries (data not shown). Our pilot SHG data has given us encouraging results, demonstrating that SHG can detect both collagen types I and III, as revealed by specific collagenase digestion for collagen types I and III in the first instance, and by double imaging, using two-photon fluorescence and SHG imaging for collagen on the same section with the histochemical method of Herovici for collagen types I and III (55) in the second instance. Here, we were able to show a very good degree of colocalization of Herovici stain and SHG, and the gradual disappearance of the SHG during collagenase digestion, revealing that collagen type III is the principle collagen type deposited in and around the wound site early on, maturing to type I as the wound resolves (data not shown). The ability of SHG to detect collagen types I and III in both forward- and backscattered geometries lends itself to use as a qualitative and possibly quantitative tool for assessing scar tissue after injury and surgery, and may be particularly useful in postoperative assessment of wounds, especially after plastic surgery. We are currently developing a miniaturized SHG microscope, relying on the backscattered signal, for use as a diagnostic tool for collagen assessment in a number of clinical conditions, including the definition of borders in malignant melanoma.

We are grateful to Professor Nicolaas Bloembergen for his helpful and supportive comments on our work. We also thank Miss Jane Pendjiky for her expert help with digital image preparation.

REFERENCES

1. Franken, P. A., A. E. Hill, C. W. Peters, and G. Weinreich. 1961. Generation of optical harmonics. *Phys. Rev. Lett.* 7:118–119.
2. Bloembergen, N. 1996. Nonlinear Optics. World Scientific Publishing, Hackensack, NJ.
3. Zernike, F., and J. E. Midwinter. 1973. Applied Nonlinear Optics. Wiley, New York.
4. Shen, Y. R. 1989. The Principles of Nonlinear Optics. Wiley, New York.
5. Yariv, A. 1991. Optical Electronics. Saunders College Publishing, Fort Worth, TX.
6. He, G. S., and S. H. Liu. 1999. Physics of Nonlinear Optics. World Scientific Publishing, Singapore.
7. Vasilenko, L. S., V. P. Chebotaev, and Yu. V. Troitski. 1965. Visual observation of infrared laser emission. *Sov. Phys. JETP*. 21: 513–514.
8. Sliney, D. H., R. T. Wangemann, J. K. Franks, and M. L. Wolbarsht. 1976. Visual sensitivity of the eye to infrared laser radiation. *J. Opt. Soc. Am.* 66:339–341.

9. Zaidi, Q., and J. Pokorny. 1988. Appearance of pulsed infrared light: second harmonic generation in the eye. *Appl. Opt.* 27:1064–1068.
10. Theodossiou, T., E. Georgiou, V. Hovhannisyan, and D. Yova. 2001. Visual observation of infrared laser speckle patterns at half their fundamental wavelength. *Lasers Med. Sci.* 16:34–39.
11. Fine, S., and W. P. Hansen. 1971. Optical second harmonic generation in biological systems. *Appl. Opt.* 10:2350–2353.
12. Roth, S., and I. Freund. 1981. Optical second harmonic scattering in rat-tail tendon. *Biopolymers.* 20:1271–1290.
13. Hochheimer, B. F. 1982. Second harmonic generation in the rabbit cornea. *Appl. Opt.* 21:1516–1518.
14. Freund, I., M. Deutsch, and A. Sprecher. 1986. Connective tissue polarity. Optical second-harmonic microscopy, crossed-beam summation and single-angle scattering in rat-tail tendon. *Biohys. J.* 50: 693–712.
15. Georgiou, E., T. Theodossiou, V. Hovhannisyan, K. Politopoulos, G. S. Rapti, and D. Yova. 2000. Second and third optical harmonic generation in type I collagen, by nanosecond laser irradiation over a broad spectral region. *Opt. Com.* 176:253–260.
16. Guo, Y., P. P. Ho, A. Triksliunas, F. Liu, and R. R. Alfano. 1996. Optical harmonic generation from animal tissues by the use of picosecond and femtosecond laser pulses. *Appl. Opt.* 35:6810–6813.
17. Hovanessian, V., and A. Lalayan. 1996. Second harmonic generation in biofibre containing tissues. *Proc. Internatl. Conf. Lasers.* 1996: 107–110.
18. Guo, Y., P. P. Ho, H. Savage, D. Harris, P. Sacks, S. Schantz, F. Liu, N. Zhadin, and R. R. Alfano. 1997. Second harmonic tomography of tissues. *Opt. Lett.* 22:1323–1325.
19. Kim, B.-M., J. Eichler, and L. B. Da Silva. 1999. Frequency doubling of ultrashort laser pulses in biological tissues. *Appl. Opt.* 38: 7145–7150.
20. Stoller, P., K. M. Reiser, P. M. Celliers, and A. M. Rubenchik. 2002. Polarization- modulated second harmonic generation in collagen. *Biophys. J.* 82:3330–3342.
21. Fraser, R. D. B., and T. P. Macrae. 1979. The crystalline structure of collagen fibrils in tendon. *J. Mol. Biol.* 127:129–133.
22. Shnyrov, V. L., V. C. Lubsandirzhieva, G. G. Zhandan, and E. A. Permyakov. 1992. Multi-stage nature of the thermal denaturation process in collagen. *Biochem. Int.* 26:211–217.
23. Miles, C. A., T. V. Burjanadez, and A. J. Bailey. 1995. The kinetics of the thermal denaturation of collagen in unrestrained rat tail tendon determined by differential scanning calorimetry. *J. Mol. Biol.* 245: 437–446.
24. Tiktopoulo, E. I., and A. V. Kajava. 1998. Denaturation of type I collagen fibrils in an endothermic process accompanied by a noticeable change in the partial heat capacity. *Biochemistry.* 37:8147–8152.
25. Rochdi, A., L. Foucat, and J. P. Renou. 1999. Effect of thermal denaturation on water-collagen interactions: NMR relaxation and differential scanning calorimetry analysis. *Biopolymers.* 50:690–696.
26. Kim, B.-M., J. Eichler, K. M. Reiser, A. M. Rubenchik, and L. B. Da Silva. 2000. Collagen structure and nonlinear susceptibility: effects of heat, glycation and enzymatic cleavage on second harmonic signal intensity. *Lasers Surg. Med.* 27:329–335.
27. Theodossiou, T., G. S. Rapti, V. Hovhannisyan, E. Georgiou, K. Politopoulos, and D. Yova. 2002. Thermally induced irreversible conformational changes in collagen probed by optical second harmonic generation and fluorescence. *Med. Sci.* (*Paris*). 17:34–41.
28. Hellwarth, R., and P. Christensen. 1974. Nonlinear optical microscopic examination of structure in polycrystalline ZnSe. *Opt. Commun.* 12: 318–322.
29. Sheppard, C. J. R., R. Kompfner, J. Gannaway, and D. Walsh. 1977. Scanning harmonic optical microscope. *IEEE J. Quantum Electron.* 13E:100D.
30. Moreaux, L., O. Sandre, and J. Mertz. 2000. Membrane imaging by second-harmonic generation microscopy. *Opt. Soc. Am. B.* 17: 1685–1694.
31. Yeh, A. T., N. Nassif, A. Zoumi, and B. J. Tromberg. 2002. Selective corneal imaging using combined second-harmonic generation and two-photon excited fluorescence. *Opt. Lett.* 27:2082–2084.
32. Campagnola, P. J., A. C. Millard, M. Terasaki, P. E. Hoppe, C. J. Malone, and W. A. Mohler. 2002. Three-dimensional high resolution second harmonic generation imaging of endogenous structural proteins in biological tissues. *Biophys. J.* 81:493–508.
33. Mohler, W., A. C. Millard, and P. J. Campagnola. 2003. Second harmonic generation imaging of endogenous structural proteins. *Methods.* 29:97–109.
34. Zoumi, A., A. Yeh, and B. J. Tromberg. 2002. Imaging cells and extracellular matrix in vivo by using second-harmonic generation and two-photon excited fluorescence. *Proc. Natl. Acad. Sci. USA.* 99: 11014–11019.
35. Cox, G., E. Kable, A. Jones, I. Fraser, F. Marconi, and M. D. Gorell. 2003. 3-Dimensional imaging of collagen using second harmonic generation. *J. Struct. Biol.* 141:53–62.
36. Brown, E., T. McKee, E. diTomaso, A. Pluen, B. Seed, Y. Boucher, and R. K. Jain. 2003. Dynamic imaging of collagen and its modulation in tumors in vivo using second harmonic generation. *Nat. Med.* 9: 786–801.
37. Dombeck, D. A., K. A. Kasischke, H. D. Vishwasrao, M. Ingelsson, B. T. Hyman, and W. W. Webb. 2003. Uniform polarity microtubule assemblies imaged in native tissue by second-harmonic generation microscopy. *Proc. Natl. Acad. Sci. USA.* 100:7081–7086.
38. Zipfel, W. R., R. M. Williams, R. Christie, A. Nikitin, B. T. Hyman, and W. W. Webb. 2003. Live tissue intrinsic emission microscopy using multiphoton-excited native fluorescence and second harmonic generation. *Proc. Natl. Acad. Sci. USA.* 12:7075–7080.
39. Deng, X., E. D. Williams, E. W. Thompson, X. Gan, and M. Gu. 2002. Second-harmonic generation from biological tissues: effect of excitation wavelength. *Scanning.* 24:175–178.
40. Hobden, M. V., and J. Warner. 1966. The temperature dependence of refractive indices of pure lithium niobate. *Phys. Lett.* 22:243–244.
41. Nath, G., and S. Haussuhl. 1969. Large nonlinear optical coefficient and phase-matched second harmonic generation in $LiIO_3$. *Appl. Phys. Lett.* 14:154–156.
42. Wang, X.-J., T. E. Milner, M. C. Chang, and J. S. Nelson. 1996. Group refractive index measurement of dry and hydrated type I collagen films using low-coherence reflectometry. *J. Biomed. Opt.* 1:212–216.
43. Maker, P. D., R. W. Terhune, M. Nisenoff, and C. M. Savage. 1962. Effects of dispersion and focusing on the production of optical harmonics. *Phys. Rev. Lett.* 8:21–22.
44. Le Calvez, A., E. Freysz, and A. Ducasse. 1998. Second harmonic field generated in reflection by an inhomogeneous nonlinear polarization. *Opt. Commun.* 145:135–140.
45. Ashkin, A., G. D. Boyd, and J. M. Dziedzic. 1963. Observation of continuous second harmonic generation with gas masers. *Phys. Rev. Lett.* 11:14–17.
46. Bolin, F. P., L. E. Preuss, R. C. Taylor, and R. J. Ference. 1989. Refractive index of some mammalian tissues using a fiber optic cladding method. *Appl. Opt.* 28:2297–2303.
47. Zernike, F., Jr. 1964. Refractive indices of ammonium dihydrogen phosphate and potassium dihydrogen phosphate between 2000 Å and 1.5 μ. *J. Opt. Soc. Am.* 54:1215–1219.
48. Shcheslavskiy, V., G. I. Petrov, S. Saltiel, and V. V. Yakovlev. 2004. Quantitative characterization of aqueous solutions probed by the third harmonic generation microscopy. *J. Struct. Biol.* 147:42–49.
49. Kurtz, S. K., and T. T. Perry. 1968. A powder technique for the evaluation of nonlinear optical materials. *J. Appl. Phys.* 39:3798–3813.
50. Chu, S.-W., S.-Y. Chen, G.-W. Chern, T.-H. Tsai, Y.-C. Chen, B.-L. Lin, and C.-K. Sun. 2004. Studies of $\chi^{(2)}/\chi^{(3)}$ tensors in submicron-scaled bio-tissues by polarization harmonics optical microscopy. *Biophys. J.* 86:3914–3922.
51. Lin, S.-J., C.-Y. Hsiao, Y. Sun, W. Lo, W.-C. Lin, G.-J. Jan, S.-H. Jee, and C.-Y. Dong. 2005. Monitoring the thermally induced structural

transitions of collagen by use of second-harmonic generation microscopy. *Opt. Lett.* 30:622–624.

52. Plotnikov, S. V., A. C. Millard, P. J. Campagnola, and W. A. Mohler. 2006. Characterization of the myosin-based source for second-harmonic generation from muscle sarcomeres. *Biophys. J.* 90: 693–703.
53. Plotnikov, S., V. Juneja, A. B. Isaacson, W. A. Mohler, and P. J. Campagnola. 2006. Optical clearing for improved contrast in second harmonic generation imaging of skeletal muscle. *Biophys. J.* 90: 328–329.
54. Qiu, C., P. Coutinho, S. Frank, S. Franke, L. Y. Law, P. Martin, C. R. Green, and D. L. Becker. 2003. Targeting connexin43 expression accelerates the rate of wound repair. *Curr. Biol.* 13:1697–1703.
55. Herovici, C. 1957. Presentation of a one-stage differential histologic staining technique; its use in cytodiagnosis. *Rev. Fr. Etud. Clin. Biol.* 2:1065–1066.